



Computational Modeling to Determine the Effect of Phenotypic Heterogeneity in Tumors on the Collective Tumor–Immune Interactions

Yuyuan Zhang¹ · Kaiqun Wang¹  · Yaoyao Du¹ · Huiyuan Yang¹ · Guanjie Jia¹ · Di Huang¹ · Weiye Chen¹ · Yanhu Shan²

Received: 2 August 2022 / Accepted: 12 April 2023 / Published online: 4 May 2023
© The Author(s), under exclusive licence to Society for Mathematical Biology 2023

Abstract

Tumor immunotherapy aims to maintain or enhance the killing capability of CD8+ T cells to clear tumor cells. The tumor–immune interactions affect the function of CD8+ T cells. However, the effect of phenotype heterogeneity of a tumor mass on the collective tumor–immune interactions is insufficiently investigated. We developed the cellular-level computational model based on the principle of cellular Potts model to solve the case mentioned above. We considered how asymmetric division and glucose distribution jointly regulated the transient changes in the proportion of proliferating/quiescent tumor cells in a solid tumor mass. The evolution of a tumor mass in contact with T cells was explored and validated by comparing it with previous studies. Our modeling exhibited that proliferating/quiescent tumor cells, exhibiting distinct anti-apoptotic and suppressive behaviors, redistributed within the domain accompanied by the evolution of a tumor mass. Collectively, a tumor mass prone to a quiescent state weakened the collective suppressive functions of a tumor mass on cytotoxic T cells and triggered a decline of apoptosis of tumor cells. Although quiescent tumor cells did not sufficiently do their inhibitory functions, the possibility of long-term survival was improved due to their interior location within a mass. Overall, the proposed model provides a useful framework to investigate collective-targeted strategies for improving the efficiency of immunotherapy.

Yuyuan Zhang and Kaiqun Wang contributed equally to the manuscript.

✉ Kaiqun Wang
wangkaiqun@tyut.edu.cn

✉ Yanhu Shan
shanyanhu@nuc.edu.cn

¹ Department of Biomedical Engineering, Research Center for Nano-Biomaterials and Regenerative Medicine, College of Biomedical Engineering, Taiyuan University of Technology, Taiyuan 030024, China

² School of Instrument and Electronics, North University of China, Taiyuan 030051, China

Keywords Quiescent tumor cells · Proliferating tumor cells · Temporal–spatial distribution · Apoptosis of tumor cells · T cell inactivation · Multi-scale model

1 Introduction

Immunotherapy, particularly immune checkpoint inhibitors (ICIs), has greatly improved the clinical efficacy of tumor treatment. However, late metastatic relapses of tumors are observed for some patients experiencing treatment and removal of the primary tumor (Phan and Croucher 2020). ICI-mediated antitumor responses depend on the capability of T cells to kill tumor cells. T cells are activated via contact with antigen-presenting cells in lymph nodes and then move close to the region of tumor mass through the circulation of blood vessels. Cytotoxic T cells release perforin/granzyme B to tumor cells in contact with them to initiate the process of apoptosis of tumor cells (Hay and Slansky 2022). Concomitantly, tumor cells start self-protection action to block the killing capability of cytotoxic T cells, such as the programmed cell death protein 1 (PD-1)/programmed death ligand 1 (PD-L1) axis, potentially leading to incomplete elimination of tumor cells (Adorisio et al. 2021). Therefore, complex interactions between tumor cells and T cells affect the fate of tumor progression.

There is growing recognition of the effect of quiescent tumor cells in solid tumors on tumor–immune interactions. Quiescent tumor cells form clusters with decreased immune infiltration and exhibit superior tumorigenic capacity as well as higher expression of stemness genes (Baldominos et al. 2022). Human solid tumor growth not only depends on rapidly proliferating cancer cells but also on the continuous production of quiescent cancer cells (Alves et al. 2018). Quiescent tumor cells exhibit stronger anti-apoptotic behaviors compared with proliferating tumor cells (Hendratta and Sudiono 2016). Moreover, the expression of PD-L1 on the surface of quiescent tumor cells is upregulated compared with proliferating counterparts (Risson et al. 2020). More than two fold PD-L1 protein expression in breast cancer stem-like cells (CSCs) is observed compared with that in non-CSCs (Hsu et al. 2018). Targeting the quiescent cell population in solid tumors facilitates to improve antitumor response. However, few studies investigate how the temporal–spatial dependent phenotypic heterogeneity affects the interactions between immune cells and a tumor mass.

Given the complexity of the tumor–immune interactions, computational models are frequently utilized to deeply explore the multi-scale responses of tumor–immune interactions. Interactions between tumor cells, dendritic cells and T cells regulated by interleukin-2 (IL-2), transforming growth factor β (TGF- β) and interleukin-10 (IL-10) are modeled based on ordinary differential equations (Robertson-Tessi et al. 2012). Interactions between tumor cells, normal tissue cells, CD4⁺ T cells, cytotoxic T-lymphocyte-associated protein 4 (CTLA-4) molecules and Interferon- γ (IFN- γ) are modeled to explore tumor dynamics and to investigate possible mechanisms of tumor regression using the ordinary differential equations (Yu et al. 2022). Given the importance of temporal–spatial tumor–immune interactions, a hybrid computational modeling is more appropriate. Of particular interest is the cellular Potts model (CPM), capable of studying of temporal–spatial behaviors of cell populations (Scianna and Preziosi 2013). The effects of the concertation of antigens and the percentage of

immunogenic cells on the interactions between tumor cells and CD8⁺ T cells are investigated based on CPM (Leschiera et al. 2022). Roy et al. develop a multi-scale model to provide insight into how cancer cells change their patterns of metabolism to compensate for the nutrient deprivation (Roy and Finley 2019). A CPM computational model is constructed to explore how alterations in cell size and deformability regulate invasiveness of the whole population of tumor cells (Asadullah et al. 2021). It is demonstrated that differential levels of 2,6-linked sialic acids enhance invasion of breast cancer epithelia via regulation of cell-ECM adhesion based on the principle of CPM (Pally et al. 2021). Hence, the CPM-based model uses an effective formalism to describe the attributes of the discrete individuals and the rules to guide the decisions of individual cells and collective dynamic interactions (Scianna and Preziosi 2012).

Based on the advantages of CPM, it is worthy to investigate the joint effect of temporal–spatial scenarios in phenotypic heterogeneity on collective tumor–immune interactions. However, some important details of the tumor–immune interactions in the context of a varying heterogeneous population of tumor cells not explicitly accounted for areas follows: First, how likely are quiescent tumor cells to emerge? It is indicated that the occasional, asymmetric loss of AKT signaling resulted in the birth of quiescent tumor cells (Dey-Guha et al. 2011; Vittadello et al. 2021). Moreover, more cells in a growing tumor mass compete for the uptake of surrounding nutrients. When the nutrients are limitedly supplied, quiescent tumor cells are more likely to be retained (Ali et al. 2021). Second, how does the temporal–spatial distribution of tumor cells with distinct states affect difference in the behaviors of tumor cells within the same population? Each tumor cell reprograms their abilities for their own individual benefit. Third, are the collective tumor–immune interactions consistent with the interactive dynamics at the single-cell level?

In this work, a CPM computational model was developed to investigate the effect of temporal–spatial scenarios in phenotypic heterogeneity on the collective tumor–immune interactions. Both the temporal–spatial distribution of glucose and the probability of asymmetric division were considered to determine the emergence of the quiescent cells in solid tumors. The fate of tumor–immune interactions depended on the collective mutual antagonism between tumor cell populations and T cell populations that was reflected in the killing of tumor cells by T cells and the inactivation of T cell activity by tumor cells. The collective tumor–immune interactions were the complex combination of behaviors of numerous single tumor-T cell pairs. Within a tumor-T cell pair, apoptosis of a tumor cell or inactivation of a cytotoxic T cell was predicted based on the responses of intracellular networks of a tumor cell which were affected by spatial distribution and types of tumor cells. The proposed model provides the underlying mechanism responsible for the tumor–immune dynamic interaction due to temporal–spatial differences in the emergence and in the function of quiescent cells within a tumor mass. Our study highlights the importance of investigating the influence of changes in a quiescence state of tumor cells in the tumor–immune interaction, providing possibility to enhance the efficiency of immunotherapy.

2 Methods

In our study, the effect of phenotypic heterogeneity of a tumor mass on collective tumor–immune interaction was quantitatively investigated based on the temporal–spatial modeling. The tempo–spatial interactions between tumor cells and T cells, in which proliferation or apoptosis of tumor cells and inactivation of T cells were involved, were characterized based on the principle of CPM. The main components of the model were consisted of tumor cells, T cells and medium. Tumor cells had three possible states: a proliferating state, a quiescent state, and a dead state. The types of T cells included activated T cells, cytotoxic T cells, inactivated cytotoxic T cells and dead T cells. Medium characterized cells within the stromal tissue and the extracellular matrix.

2.1 The CPM Modeling Framework of Tumor–Immune Interactions

To model the dynamics of tumor cells and T cells, the effective energy H was applied to characterize attributes, behaviors, and interactions of cells based on the principle of CPM, as follows:

$$H = H_{\text{vol}} + H_{\text{surf}} + H_{\text{chemo}} + H_{\text{adh}} \quad (1)$$

where H_{vol} and H_{surf} are indicative of the energy associated with changes in volume and surface area of cells; H_{chemo} denotes the effective energy related with chemotaxis due to the concentration gradients of glucose for tumor cells or motility-related chemokine for T cells; H_{adh} reflects the adhesion energy between cells.

$$H_{\text{vol}} = \sum_{\sigma} \lambda_{\sigma}^{\text{vol}} (v_{\sigma} - V_{\sigma})^2 \quad (2)$$

$$H_{\text{surf}} = \sum_{\sigma} \lambda_{\sigma}^{\text{surf}} (s_{\sigma} - S_{\sigma})^2 \quad (3)$$

$$H_{\text{chemo}} = -\lambda_{\text{chemo}} (C_j - C_i) \quad (4)$$

$$H_{\text{adh}} = \sum_{i,j} J(\tau(\sigma_i), \tau(\sigma_j)) (1 - \delta(\sigma_i, \sigma_j)) \quad (5)$$

where $\lambda_{\sigma}^{\text{vol}}$ is the inverse compressibility of the cell; v_{σ} is the current volume of the cell; V_{σ} is the target volume of the cell; $\lambda_{\sigma}^{\text{surf}}$ is the inverse membrane compressibility; s_{σ} is the current surface area of the cell; S_{σ} is the target surface area of the cell; λ_{chemo} represents the chemotactic coefficient; C_{ij} is the concentration of chemotactic field at the specific pixel; J denotes the adhesion energy between different cells; δ is the Kronecker delta; τ is the cell type; σ is cell ID; i and j are lattice sites.

The evolvement of cell configuration was determined by stochastic pixel-copy attempts to minimize the effect energy. Based on the principle of the CPM, changes in the effective energy were implemented pixel-copy attempt (Swat et al. 2012; Guisoni et al. 2018). During each attempt, the index i of a source pixel from the cell lattice of a

cell was randomly selected and then the index j of a target pixel from its neighboring pixels was randomly selected. If the source pixel and the target pixel did not belong to the same cell, the cell containing the source pixel attempted to occupy the target pixel with a certain probability related with changes in the effective energy. If they belonged to the same cell, the pixel-copy attempt did not occur. At each time step, the total number of pixels of cells was randomly chosen and the probability of the configuration update of a cell was evaluated. The number of attempts was determined by the total number of pixels of all cells at each step and the positions of pixels. Cell dynamics in the CPM model were implemented using a stochastic modified Metropolis algorithm consisting of a series of pixel-copy attempts. The pixel changes were accepted or rejected with a probability (P) that depended on the changes in effective energy as follows. Therefore, the CPM favored changes that decreased the effective energy of the system (Rens and Edelstein-Keshet 2019).

$$P = \begin{cases} 1, & \Delta H \leq 0 \\ e^{-\frac{\Delta H}{T_m}}, & \Delta H > 0 \end{cases} \quad (6)$$

where ΔH denotes alterations in the effective energy resulting from the occurrence of copy attempts and T_m is a parameter characterizing the amplitude of fluctuations of cell membrane.

The model mainly consisted of three modules with the schematic of rules for the tumor-immune interactions shown in Fig. 1. The first module described growth, division and changes in quiescent level of a tumor mass determined both by asymmetric division and by the concentration of glucose (Fig. 1a). The second module displayed transitions from activated T cells to cytotoxic T cells and the evaluation of their lifespan (Fig. 1b). The third module described the apoptosis of tumor cells with different types induced by cytotoxic T cells and inactivation of cytotoxic T cells due to the PD-L1 expression of tumor cells (Fig. 1c).

2.2 Model Rule I: State Transition of Tumor Cells Regulated by Glucose and Asymmetric Division

36 quiescent tumor cells were initially located in the center of the simulation domain. Within the simulation domain, glucose was supplied by the blood vessels in stromal tissue represented by cells with the type of medium. Glucose was modeled as extracellular continuous fields via partial differential equations (PDEs). Given the distinct diffusion constants of continuous field in the model, the CompuCell3D (CC3D) steady-state diffusion-equation solver was appropriate for a fast-diffusing species like glucose based on the Helmholtz equation (Roy and Finley 2019). Dynamic distribution of glucose at each pixel was calculated as Eq. (7). The secretion and diffusion rates of glucose were fixed with the values derived from existing references (Swat et al. 2015).

$$\frac{\partial C_{\text{glu}}}{\partial t} = D_{\text{glu}} \nabla^2 C_{\text{glu}} - k_{\text{decay_glu}} C_{\text{glu}} - \delta_{\text{PT}} \frac{u_{\text{max_PT}} C_{\text{glu}}}{C_{\text{glu}} + K_{\text{PT}}} - \delta_{\text{QT}} \frac{u_{\text{max_QT}} C_{\text{glu}}}{C_{\text{glu}} + K_{\text{QT}}} + k_{\text{pro_glu}} N_{\text{medium}} \quad (7)$$

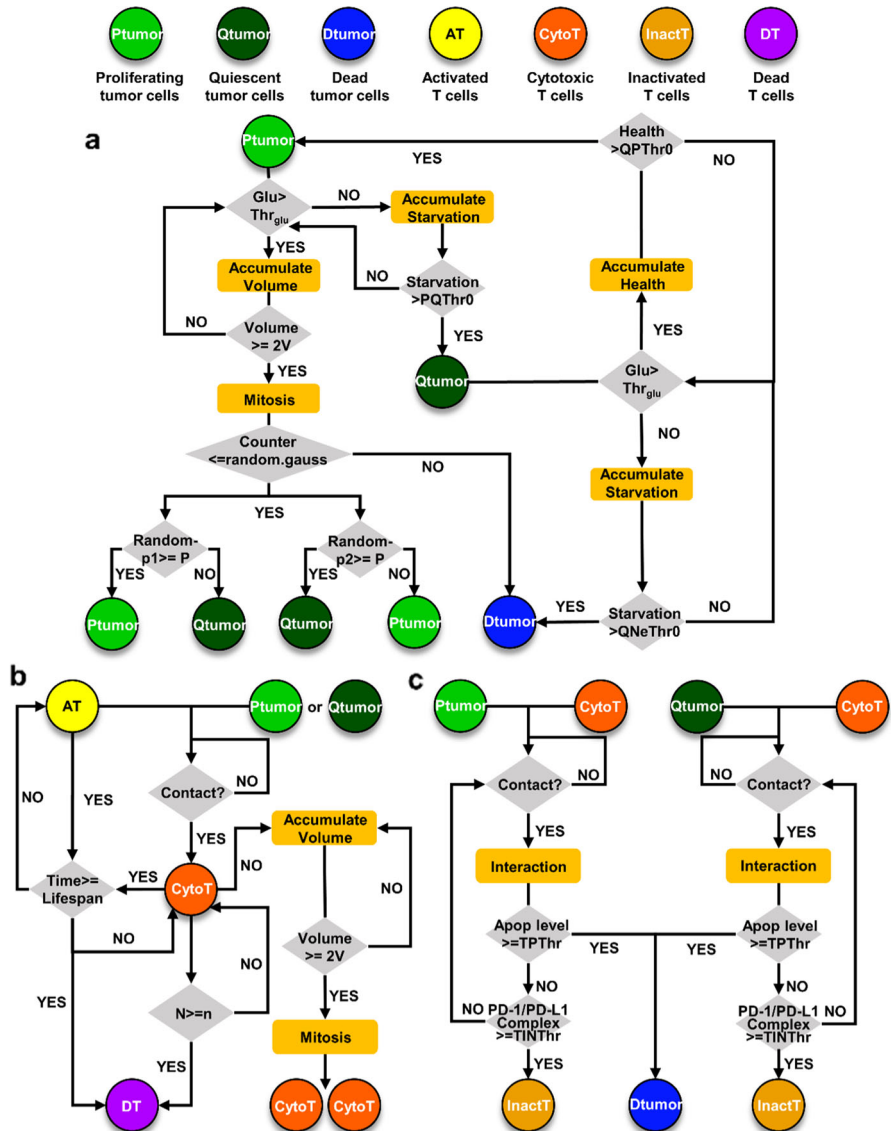


Fig. 1 The schematic of model rules for the tumor-immune interactions. **a** Model rule I: state transition of tumor cells regulated by glucose and asymmetric division; **b** Model rule II: formation of cytotoxic T cells and their lifespan; **c** Model rule III: tumor-immune interactions

where D_{glu} is the diffusion coefficient of glucose; $k_{\text{decay_glu}}$ is the degradation rate of glucose; $k_{\text{pro_glu}}$ denotes the secretion rate of glucose by medium; δ_{PT} equals one only at pixels occupied by proliferating tumor cells, δ_{QT} equals one at pixels occupied by quiescent tumor cells, otherwise; both δ_{PT} and δ_{QT} equal zero; $u_{\text{max_PT}}$ and $u_{\text{max_QT}}$ are the maximum uptake rates of proliferating tumor cells and quiescent tumor cells,

respectively; K_{PT} and K_{QT} are Michaelis–Menten constants of the local glucose concentration C_{glu} for proliferating tumor cells and quiescent tumor cells, respectively; N_{medium} is the number of medium in the simulation domain.

Tumor cells sensed the concentration of glucose and then continued to migrate, grow, or divide. The glucose field gradient within the simulation domain drove living tumor cells to migrate toward the region of sufficient glucose. When the glucose uptake concentration C_{glu} of the center of mass of quiescent tumor cells was higher than the starvation threshold $GluD$, tumor cells would accumulate health factors. The accumulated health factor was calculated as Eqs. (8–9). If the health factor of a quiescent tumor cell was above the threshold $QPThr0$, it would switch from a quiescent state to a proliferating state. On the contrary, a tumor cell with proliferating or quiescent states accumulated starvation damage as a form mentioned in Eqs. (10–11), and then it would correspondently become a quiescent cell or a dead cell. The growth of proliferating tumor cells was regulated by the distribution of glucose and characterized by the difference between the current volume and the target volume. Increments of the target volume of proliferating tumor cells were proportional to the difference between local changes in the concentration of glucose at the cells' center of mass and growth threshold associated with glucose at each step (Eq. 12).

$$\Delta F = \begin{cases} \frac{mC_{glu}}{C_{glu}+K} - \frac{mGluD}{GluD+K}, & \text{for } C_{glu} \geq GluD \\ 0, & \text{for } C_{glu} < GluD \end{cases} \quad (8)$$

$$F_{current} = F_{previous} + \Delta F \quad (9)$$

$$\Delta S = \begin{cases} 0, & \text{for } C_{glu} \geq GluD \\ \frac{mGluD}{GluD+K} - \frac{mC_{glu}}{C_{glu}+K}, & \text{for } C_{glu} < GluD \end{cases} \quad (10)$$

$$S_{current} = S_{previous} + \Delta S \quad (11)$$

$$V_{current_target} = V_{previous_target} + k_{growth}(C_{glu} - Thr_{glu}) \quad (12)$$

where m is the maximum uptake rate of glucose of each tumor cell and K is a Michaelis–Menten constant; $V_{current_target}$ is the target volume of proliferating tumor cells at the current step; $V_{previous_target}$ is the target volume of proliferating tumor cells at the previous step; k_{growth} is the growth rate of proliferating tumor cells; Thr_{glu} is the growth threshold.

When a proliferating tumor cell reached as twice as their initial volumes, it started to divide. Given the occasional loss of AKT signaling, probability-controlled asymmetric division of a tumor cell also resulted in the random birth of quiescent tumor daughter cells in our model. Changes in the probability of asymmetric division affected the emergence of quiescent tumor cells or even the total number of tumor cells, which then triggered the global or local consumption of glucose and further mediated the number and the distribution of tumor cells with different phenotypes. Such kind of chain responses made the temporal–spatial effect of quiescent tumor cells on collective tumor–immune interactions more complex. We set probability of asymmetric division

of proliferating tumor cells as 0.3, 0.5 and 0.8 in six independent cases, respectively, indicating higher potential of emergence of quiescent tumor cells in a tumor mass. It was assumed that all proliferating tumor cells have the same probability of division in one simulation. Taken together, the joint effect of asymmetric division and glucose on changes in the number and distribution of tumor cells, especially in a quiescent state, provided the clues for the changes in tumor–immune interactions.

2.3 Model Rule II: Formation of Cytotoxic T Cells and Their Lifespan

It was assumed that there was sufficient vascularization for recruitment of T cells. Two activated T cells were recruited every time step with basal recruitment rate independent with the number of living tumor cells because of limited number of living tumor cells on the discrete cellular level (de Pillis and Radunskaya 2014; Gong et al. 2017). The lifespan of a T cell was about 41 h, at which point it died (Kim and Lee 2012). Recruited activated T cells randomly appeared in available sites on the lattice of the “medium-type” region to characterize the fact that the entry of activated T cells to the tumor microenvironment was associated with tumor vessel density and perfusion. The region of cells with the type of medium represented the blood vessels in stromal tissue (Cess and Finley 2020). Activated T cells moved randomly in no particular direction within the simulation domain based on the pixel copy attempts. When contacted with tumor cells, they were transformed into cytotoxic T cells (effector T cells). The tumor–effector complexes secreted chemokine in order to attract more surrounding activated T cells toward the tumor region via chemotaxis (Cooper and Kim 2014). The distribution of chemokine within the simulation domain was described in Eq. (13), using the CC3D kernel diffusion solver. When initially randomly motile activated T cells perceived chemokine, their motility was dominantly controlled by the strength of chemotaxis. Subsequently, those activated T cells exhibited a directed movement pattern due to the higher proportion of chemotaxis-induced effective energy. When the tumor cell in a complex died, the complex was replaced by only the effector T cell, and then secretion of chemokine stopped. The entry of activated T cells to this region led to switch from a random walk to a directed walk. The rules determined the fates of a tumor cell and a cytotoxic T cell.

$$\frac{\partial C_{\text{chem}}}{\partial t} = D_{\text{chem}} \nabla^2 C_{\text{chem}} - k_{\text{decay_chem}} C_{\text{chem}} + k_{\text{pro_chem}} T_{\text{pair}} \quad (13)$$

where D_{chem} is the diffusion coefficient of chemokine; $k_{\text{decay_chem}}$ is the degradation rate of chemokine; $k_{\text{pro_chem}}$ denotes the secretion rate of chemokine by tumor cells in the tumor–effector complexes; T_{pair} denotes the amount of the tumor–effector complexes.

2.4 Model Rule III: Tumor–Immune Interactions

The interactions between cytotoxic T cells and tumor cells were associated with apoptotic behaviors of tumor cells induced by cytotoxic T cells and inactivation of cytotoxic

T cells due to PD-L1 expression of tumor cells. The apoptotic process of tumor cells induced via the function of perforin/granzyme B released by cytotoxic T cells. Quiescent tumor cells expressed high level of B-cell lymphoma-2 (Bcl-2), the anti-apoptosis protein (Phan and Croucher 2020). Thus, quiescent tumor cells exhibited stronger anti-apoptotic behaviors than proliferating tumor cells with exposure to the same amount of perforin/granzyme B. The difference in the cellular-level anti-apoptotic capabilities of quiescent tumor cells and proliferating tumor cells characterized by the intracellular apoptotic level was quantitatively described based on ordinary differential equation (ODE) model by setting different concentration values of Bcl-2 (Supplementary material 1). The Bcl-2-related intracellular dynamic changes in apoptotic level of tumor cells were updated every Monte Carlo Step (MCS). If the apoptosis level of tumor cells was greater than their threshold, tumor cells could be killed by cytotoxic T cells.

Tumor cells could perform the function of the inactivation of cytotoxic T cells via the combination of PD-1 (T cells) and PD-L1 (tumor cells), if they were not killed by cytotoxic T cells. The dynamic concentrations of PD-L1 were shown around the surface of tumor cells at the cellular level responsible for blocking the functions of cytotoxic T cells in contact with PD-L1+ tumor cells. If the concentration of the PD-1/PD-L1 complexes was above the threshold, cytotoxic T cells would be inactivated. Compared with proliferating tumor cells, quiescent tumor cells had higher capabilities of PD-L1 expression with exposure to the same strength of IFN- γ induction (Hsu et al. 2018; Risson et al. 2020). The IFN- γ -induced PD-L1 expression of tumor cells was modeled based on a set of ODEs (Supplementary material 1). The intracellular dynamic changes in PD-L1 level of tumor cells were updated every MCS. The distinct abilities of quiescent tumor cells and proliferating tumor cells to express PD-L1 was associated with PD-L1 *N*-glycosylation and was reflected in the process of interferon regulatory factor 1 (IRF-1)-mediated PD-L1 production by setting distinct Michaelis constants (Kleffel and Schatton 2013). The cellular-level PD-L1 concentration of tumor cells was determined by their phenotype-dependent expression capacity and the uptake concentration of IFN- γ from the surrounding environment. Distribution of IFN- γ was calculated at each pixel within the simulation domain (Eq. 14) using the CC3D kernel diffusion solver (Gao et al. 2016).

$$\frac{\partial C_{\text{IFN}}}{\partial t} = D_{\text{IFN}} \nabla^2 C_{\text{IFN}} - k_{\text{decay_IFN}} C_{\text{IFN}} + k_{\text{pro_IFN}} N_{\text{CYC}} \quad (14)$$

where D_{IFN} is the diffusion coefficient of IFN- γ ; $k_{\text{decay_IFN}}$ is the degradation rate of IFN- γ ; $k_{\text{pro_IFN}}$ denotes the production rate of IFN- γ ; N_{CYC} is the number of cytotoxic T cells.

Cells in the domain of simulation were considered as discrete entities with attributes of type, volume, surface area, adhesion, and chemotaxis. The dimension of the simulation domain in pixels was $250 \times 250 \times 1$. Both dimensions of tumor cells and cytotoxic T cells in pixels were $4 \times 4 \times 1$. One pixel in the simulation was set to $4 \mu\text{m}$. The whole simulation domain represented a $1.0 \text{ mm} \times 1.0 \text{ mm}$ tissue slice. The correspondence of real time to one MCS is 24 min in our model in order to balance the computational expense for each scenario simulated with the capture of the details of multi-scale changes. Tumor evolution was simulated for 2000 MCS (about 33 days),

covering a time period of tumor–immune interaction mentioned in the previous studies (Radunskaia et al. 2018; Benchaib et al. 2019). The model was implemented using CC3D. The parameters of the cellular model are shown in Table 1. All quantitative results were expressed as means \pm standard deviation. Student's *t* significance test was used to evaluate the statistical difference between the groups. Statistical differences were set at *: $P < 0.05$; **: $P < 0.01$; ***: $P < 0.001$. All experiments were performed in six iterations.

3 Results and Discussion

3.1 The Modeling Outline of the Tumor–Immune Interactions

Figure 2a illustrates the simulated outline of the model of the tumor–immune interactions. Transition of tumor cells between a quiescent state and a proliferating state was regulated by the distribution of glucose and asymmetric division (Fig. 2b). Activated T cells were recruited by tumor cells and then moved toward the region of a tumor mass due to effect of chemotaxis, shown in Fig. 2c. Activated T cells were transformed into cytotoxic T cells when they contacted with tumor cells. Dynamics of tumor–immune interactions were dependent on mutual antagonism between tumor cells and cytotoxic T cells. Proliferating tumor cells and quiescent tumor cells exhibited non-uniform suppressive roles in activity of cytotoxic T cells. Meanwhile, proliferating tumor cells and quiescent tumor cells had distinct anti-apoptotic responses to killing of cytotoxic T cells. Mutual antagonisms between tumor cells and cytotoxic T cells were incorporated with intracellular behaviors of tumor cells in order to reflect the temporal–spatial heterogeneity in tumor–immune interactions. The effects of intracellular rules of PD-L1 expression and apoptosis of an individual tumor cell on cellular behaviors are demonstrated in Fig. 2d, e.

3.2 Model Validation

The developed model elaborated how heterogeneous phenotypes of tumor cells regulated the tumor immunity in different temporal–spatial domains. In all cases, we ran the model multiple times for each setting in order to capture the stochasticity in CompuCell3D. We chose 6 iterations for each case to balance the computational expense for each scenario simulated with the stochasticity in the model simulation. In Fig. S1, the black solid lines are the mean of 6 simulations and 18 simulations, respectively, with the shaded grey areas representing the standard deviation of the simulations. It was confirmed that additional simulations did not exhibit unusual behaviors because of similar trend of the mean volume of a tumor mass and narrow standard deviations. The model was validated by comparing the previous studies. Some physiologically reasonable criteria were utilized to validate our model quantitatively and qualitatively (Fig. 3): first, the rate of tumor growth depended on cell types (Grimes et al. 2016; Wen et al. 2013; Semba et al. 2004; Tysnes et al. 2001). The changes in volume fold of tumor growth in the proposed model were within the range of experimental results (Fig. 3a),

Table 1 Model parameters

Symbol	Parameter	Value	References
D_{glu}	Diffusion coefficient of the glucose	45,000 voxel ² /MCS	Roy and Finley (2019)
$k_{\text{decay_glu}}$	Degradation of the glucose	6.248/MCS	Roy and Finley (2019)
$k_{\text{pro_glu}}$	Secretion rate of the glucose by medium	2 fmol/voxel/cell/MCS	Roy and Finley (2019)
$u_{\text{max_PT}}$	Maximum uptake rates of P_{tumor}	9 fmol/voxel/MCS	Swat et al. (2015)
$u_{\text{max_QT}}$	Maximum uptake rates of Q_{tumor}	6.76 fmol/voxel/MCS	Swat et al. (2015)
K_{PT}	Michaelis constants of the local glucose concentration for P_{tumor}	0.00256 fmol/voxel	Swat et al. (2015)
K_{QT}	Michaelis constants of the local glucose concentration for Q_{tumor}	0.00256 fmol/voxel	Swat et al. (2015)
k_{growth}	Growth rate of P_{tumor}	2 pixels/MCS	Roy and Finley 2019; Swat et al. (2015)
Thrglu	Growth threshold	0.032 fmol/voxel	Swat et al. (2015)
GluD	Starvation threshold	0.032 fmol/voxel	Swat et al. (2015)
PQThr0	Threshold of transition from P_{tumor} to Q_{tumor}	102 fmol/voxel	Assumed
QNeThr0	Threshold of transition from Q_{tumor} to D_{tumor}	204 fmol/voxel	Swat et al. (2015)
QPThr0	Threshold of transition from Q_{tumor} to P_{tumor}	79.5 fmol/voxel	Swat et al. (2015)
p	Asymmetric mitotic probability	0.3, 0.5, 0.8	Vittadello et al. (2021)
D_{chem}	Diffusion coefficient of Chemokine	1080 voxel ² /MCS	Cooper and Kim (2014)
$k_{\text{decay_chem}}$	Degradation of Chemokine	0.0336/MCS	Cooper and Kim (2014)
$k_{\text{pro_chem}}$	Production rate of Chemokine	24 nM/cell/MCS	Cooper and Kim (2014)
λ_{chemo}	Chemotactic coefficient for T cells due to the effect of chemokine	120	Cooper and Kim (2014)
	Chemotactic coefficient for tumor cells due to the effect of glucose	500	Swat et al. (2015)
D_{IFN}	Diffusion coefficient of IFN- γ	130.2 voxel ² /MCS	Liao et al. (2014)
$k_{\text{decay_IFN}}$	Degradation of IFN- γ	0.036/MCS	Liao et al. (2014)
$k_{\text{pro_IFN}}$	Production rate of IFN- γ	0.572 nM/cell/MCS	Liao et al. (2014)

Table 1 (continued)

Symbol	Parameter	Value	References
TPThr	Threshold of tumor apoptotic by cytotoxic T cells	100 nM	Kim and Lee (2012)
TINThr	Threshold of T cell activity inhibition by the complex	0.05 nM	Assumed
T cell	T cell lifespan	102.5 MCS	Kim and Lee (2012)
	Times for T cell to kill tumor cell	5 tumor cells	Kather et al. (2017)

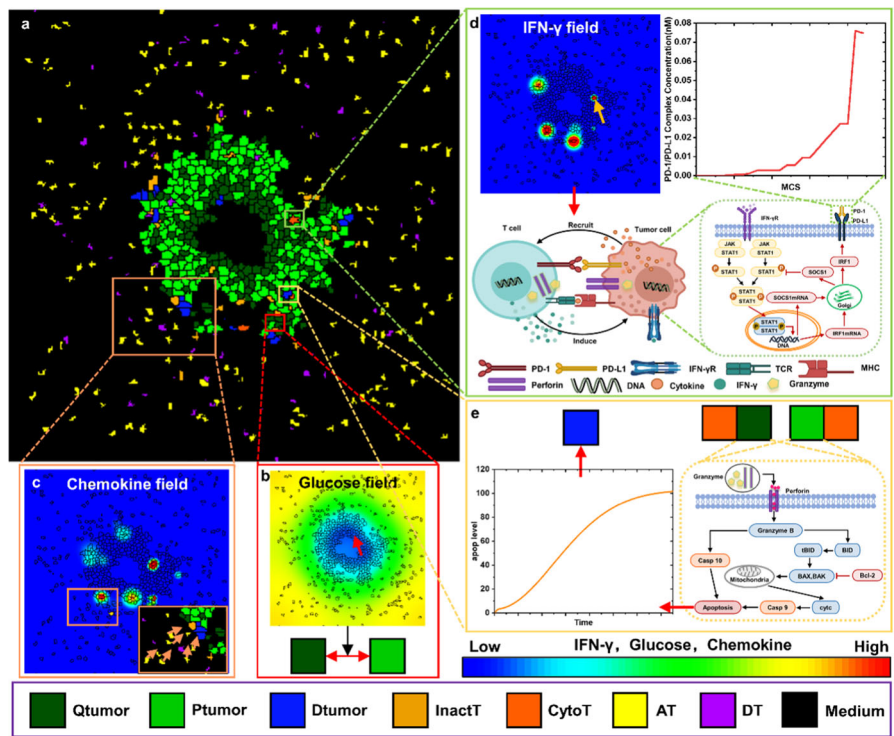


Fig. 2 The simulated outline of the multi-scale model of tumor-immune interactions. **a** The cellular-level profile of the model; **b** Model interaction rule I: Cell state transition regulated by glucose and asymmetric division; **c** Model interaction rule II: Chemotaxis of activated T cells; **d** Model interaction rule III: the inactivation of cytotoxic T cells induced by tumor cells; **e** Model interaction rule III: the apoptosis of tumor cells attacked by cytotoxic T cells

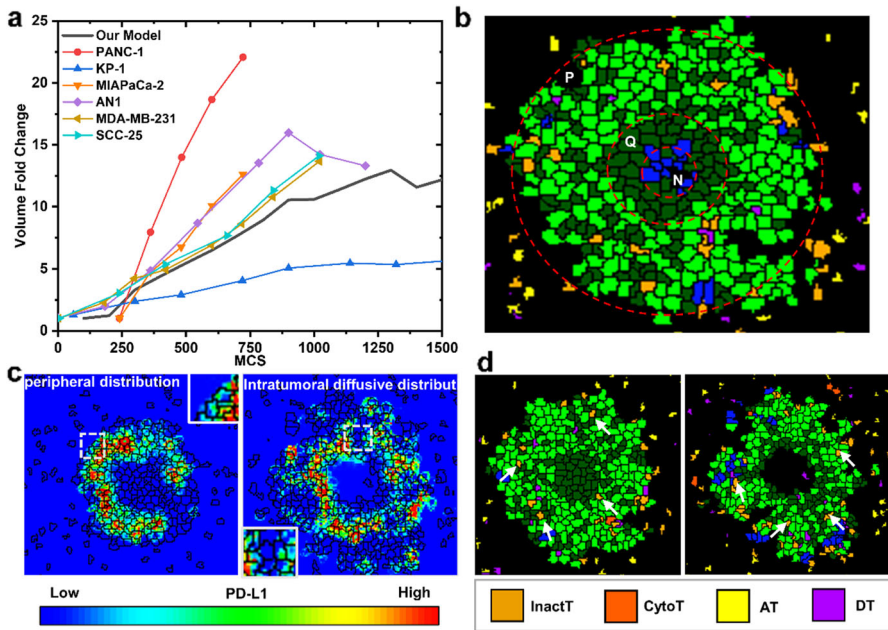


Fig. 3 The proposed model was validated based on previous experimental data. **a** Comparison of changes in the volume fold of a tumor mass in our model with experimental data: KP-1 cells (Semba et al. 2004), PANC-1 cells and MIAPaCa-2 cells (Wen et al. 2013), AN-1 cells (Tysnes et al. 2001), MDA-MB-231 cells and SCC-25 cells (Grimes et al. 2016); **b** comparison of the patterns of the distribution of proliferating, quiescent and necrotic tumor cells in our model with experimental data (Zhang et al. 2015); **c** comparison of PD-L1 distribution in our model with experimental data (Lyford-Pike et al. 2013; Phillips et al. 2015); **d** comparison of the status of infiltrating T cells within a tumor mass with experimental data, infiltrating cytotoxic T cells partially inactivated in tumor cells were shown by white arrows (Liu et al. 2020; Granier et al. 2018)

especially according with the results of the breast cancer line and the squamous cell carcinoma line (Grimes et al. 2016). Second, the distributions of tumor cells with different states (Fig. 3b), such as proliferating, quiescent and necrotic states, were similar to those reported in previous studies (Zhang et al. 2015). Deficiency of glucose made tumor cells in the core turn into necrotic cells and then necrotic tumor cells shrank and eventually disappear by decreasing their target volume to zero at a constant shrinkage rate. The development of a necrotic core was shown to be an important feature of tumor spheroids. Our model simulations reproduced this feature. Third, the work of Lyford-Pike's group demonstrated two distinct distribution patterns of PD-L1+ tumor cells, including the peripheral of a tumor mass and the diffusive intratumoral region by utilizing the approach of immunohistochemistry to mark the distribution of PD-L1. In Fig. 3e, f of their work (Lyford-Pike et al. 2013), dark brown dots represent PD-L1 expression. In Fig. 3c of our work, PD-L1 expression from low to high is shown in blue, green, yellow and red. The left figure exhibits relatively high PD-L1 expression (shown in green and red) was found in the mode of peripheral distribution. The right

figure shows PD-L1 was expressed in a diffusive mode within a tumor mass. Therefore, our model was qualitatively validated by comparing similar PD-L1 distribution of the experimental tasks. Fourth, the work of Liu's group mentioned the frequency of inactivated T cells was increased in the tumor core (Liu et al. 2020). Figure 3d indicates the status of infiltrating T cells within the region of a tumor mass. Infiltrating T cells were displayed in orange. During different stages of tumor growth, most infiltrating T cells were in an inactivated state. Therefore, our model was qualitatively consistent with the conclusion of Liu's work.

3.3 The Cellular-Level Profiles of Tumor–Immune Interactions Triggered by Asymmetric Division

At cellular level, more complicated tumor–immune interactions could be observed within a heterogeneous population of tumor cells. Asymmetric tumor cell division could lead to uncertainty in the types of tumor cells that interacted with T cells. Competition between tumor cells for nutrient consumption further led to redistribution of tumor cells with various types. Figure 4 shows the cellular-profiles of tumor–immune interactions triggered by different division probability. As the time went on, more quiescent tumor cells resided in the interior region of the tumor mass. Tumor cells at the periphery had higher possibility to absorb more glucose and contact with cytotoxic T cells. Increase of p yielded more quiescent tumor cells which had the lower uptake rate of the nutrient, leading to gently stable consumption of glucose in the domain. More finger-like shapes could be observed at the periphery of the tumor mass (Fig. 5a). The appearance of concave regions (indicated by red arrows) could enhance the probability of contact of quiescent tumor cells in the interior of the tumor mass with cytotoxic T cells to some extent. As indicated in Fig. 5b, the tumor mass was the largest when the parameter p was 0.3 until 500 MCS. A greater tumor mass, especially with more proliferating tumor cells ($p = 0.3$), consumed more glucose compared with the case of p with the values of 0.5 and 0.8. After 1200 MCS, the volume of a tumor mass ($p = 0.3$) decreased at a slow rate. Increased p promoted higher proportions of quiescent tumor cells, leading to the moderate consumption of glucose and the slow and steady growth of a tumor mass. Given more proliferating tumor cells in the case that p was 0.5 than those when p was 0.8, the growth rate ($p = 0.5$) was faster than that in the case of p with value of 0.8. Excessive consumption of glucose could result in the emergence of the necrotic areas. Changes in the necrotic areas of the tumor mass are shown in Fig. 5c. At 1000 MCS, the necrotic area was larger when p was 0.3 than that when p was 0.5, while no necrotic cells could be observed due to an almost adequate supply of glucose in the case of p with the value of 0.8. The necrotic area of a tumor mass initially experienced a swell and then shrank ($p = 0.3$) due to the initial excessive consumption of glucose. A reduced-sized tumor mass resulted in the gradual recovery of glucose supply followed. Increased p yielded the gradual increase of the necrotic areas on account of the slowly continuous consumption of glucose.

When more T cells contacted with the tumor cells at the margin of the mass, activated T cells were transformed into cytotoxic T cells. The outcome of the tumor–immune interactions was determined by the antagonism between tumor cells and cytotoxic

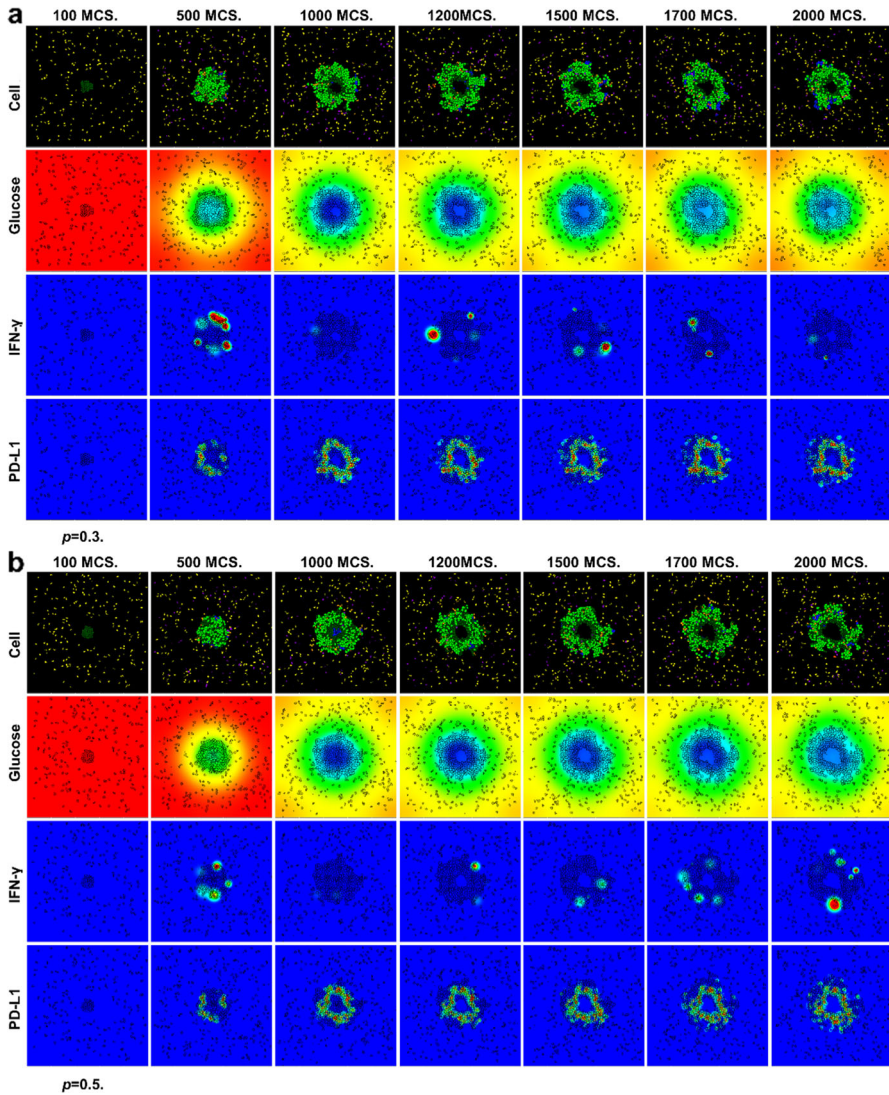


Fig. 4 The tumor–immune interactions with different probabilities of asymmetric division. **a** $p = 0.3$; **b** $p = 0.5$; **c** $p = 0.8$

T cell. A larger tumor mass supported broader contact surface with more cytotoxic T cells which secreted higher amount of IFN- γ , inducing more PD-L1 expressed on tumor cells at the periphery of the mass. The tumor mass grew outward, original proliferating tumor cells could become quiescent tumor cells due to limited nutrient or probabilistic division, so the expression of PD-L1 was then mostly concentrated in the interior region of a tumor mass. Spot-like patterns of the expression of PD-L1 could be shown at the periphery of the tumor mass when tumor cells contacted with

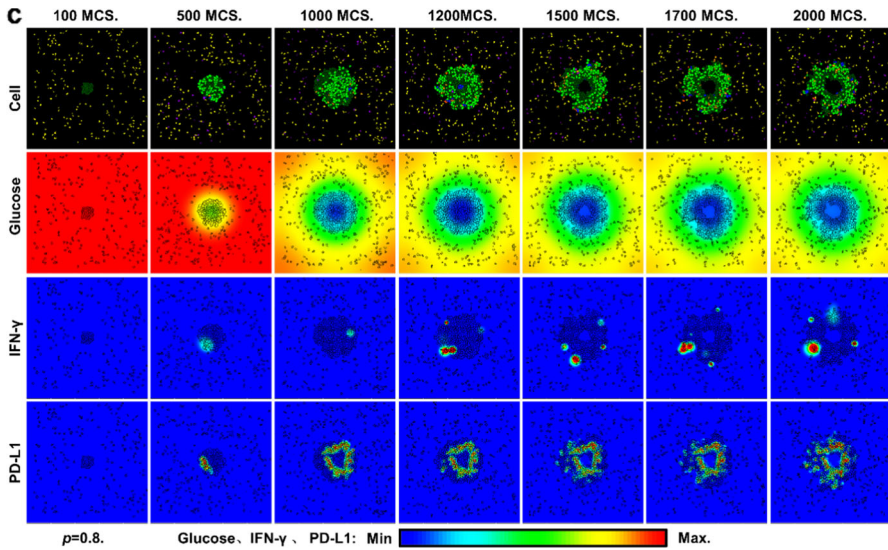


Fig. 4 continued

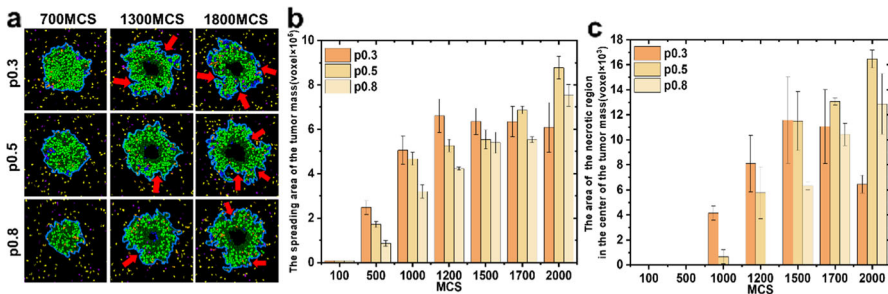


Fig. 5 **a** The outline of a tumor mass; **b** the spreading area of a tumor mass; **c** the area of the necrotic region

cytotoxic T cell. Moreover, the cell-type switch to a quiescent state during the process of mitosis could further improve the expression of PD-L1 at the periphery of the tumor mass (Fig. 4). Meanwhile, cytotoxic T cells released perforin/granzyme B to initiate the process of apoptosis of tumor cells. If the apoptotic threshold was reached, tumor cells were transformed into apoptotic cells, shown in the cell fields of Fig. 4. The more detailed information of tumor-immune interactions could be explained in the following parts.

3.4 The Difference in the Cellular-Level PD-L1 Expression Between a Population of Proliferating Tumor Cells and a Population of Quiescent Tumor Cells

The number, the cell-type proportion and the total amount of PD-L1 expression of living tumor cells contributed to the collective inhibitory function of a tumor mass. Figure 6a illustrates that the number of living tumor cells ($p = 0.3$) gradually increased to its maximum value until around 750 MCS and then slightly decreased, consistent with Fig. 5b. As the increase of p , the number of living tumor cells reached greater maximum values with a certain time delay. Among all living tumor cells, increased p made tumor cells presumably divide toward a quiescent state, indicated in Fig. 6b, c. Before 1000 MCS, obvious oscillation in the number of living quiescent tumor cells ($p = 0.8$) resulted from rapid switch between a proliferating state and a quiescent state. The rapid switch could be explained by the facts of tumor cells division toward a quiescent state and then immediate switch from a quiescent state to a proliferating

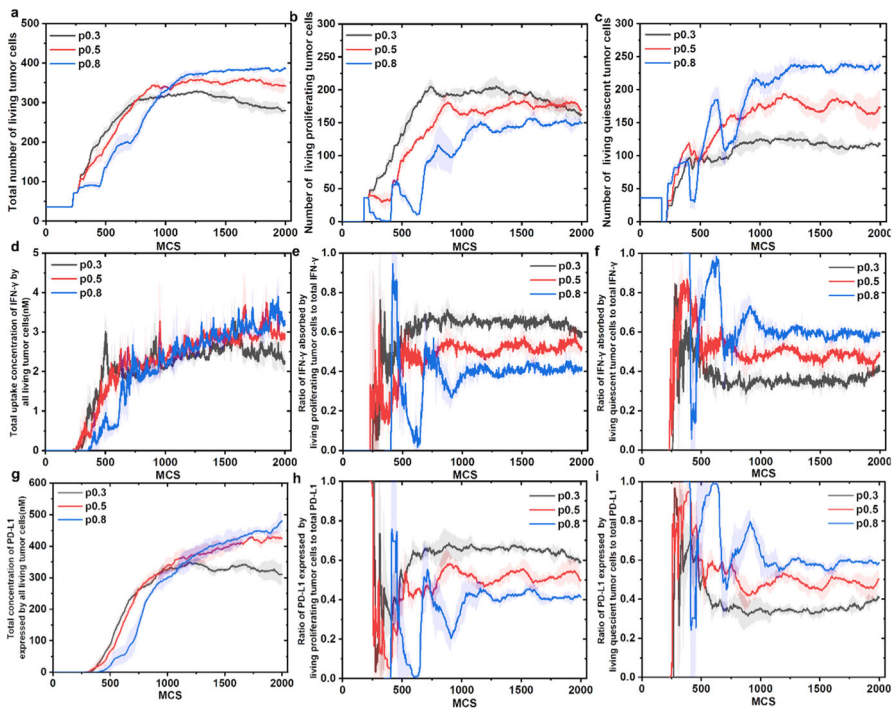


Fig. 6 Dynamic changes in the number of living tumor cells for different probabilities of asymmetric division. The first row indicates the cases of living tumor cells: **a** the total number of living tumor cells; **b** the number of living proliferating tumor cells; **c** the number of living quiescent tumor cells. The second row indicates the cases of IFN- γ : **d** The total concentration of IFN- γ absorbed by all living tumor cells; **e** ratio of uptake of IFN- γ by proliferating tumor cells to total uptake of IFN- γ ; **f** ratio of uptake of IFN- γ by quiescent tumor cells to total uptake of IFN- γ . The third row indicates the cases of PD-L1: **g** the total concentration of PD-L1 expressed by all living tumor cells; **h** ratio of expression of PD-L1 by proliferating tumor cells to total expression of PD-L1; **i** ratio of expression of PD-L1 by quiescent tumor cells to total expression of PD-L1

state due to sufficient glucose supply. After 1000 MCS, as the increase of the number of tumor cells, glucose was supplied limitedly, so the fate of quiescent tumor cells was stable resulting from three sources: (1) the switch from a proliferating state to a quiescent state; (2) maintaining their resting state; (3) the switch to a necrotic state.

As illustrated in Fig. 4, IFN- γ was heterogeneously distributed within the simulation domain. To better understand the differences in the suppressive functions between a population of proliferating tumor cells and a population of quiescent tumor cells, it was essential to focus on the uptake amount of IFN- γ by living tumor cells, especially by two heterogeneous populations (Fig. 6d). Within the whole simulation domain, no significant diversity of the total amount of IFN- γ could be observed for the cases of p with the values of 0.3, 0.5 and 0.8. Consider the differences in the number of living tumor cells shown in Fig. 6a–c, it could be concluded that there was an existing difference between the capacities of two populations of tumor cells to absorb IFN- γ . The increased number of quiescent tumor cells did not guarantee the equally increased proportion of IFN- γ absorption (Fig. 6e, f). Although quiescent tumor cells had a higher potential of PD-L1 expression determined by the intracellular network, limited IFN- γ absorption caused that PD-L1 expression of a population of quiescent tumor cells did not increase as much as the number of cells increased under the case of increased p (Fig. 6g–i). The distribution of quiescent tumor cells, shown in Fig. 4, determined whether a tumor mass with high proportion of quiescent tumor cells could adequately play its role in inactivating cytotoxic T cells. In the following part, the suppressive roles of a tumor mass with distinct proportion of quiescent tumor cells were investigated.

3.5 The Difference in Collective Suppressive Efficiency of a Population of Proliferating Tumor Cells and a Population of Quiescent Tumor Cells

The collective suppressive effects of tumor cells on cytotoxic T cells were characterized by changes in the number of inactivated T cells. Phenotypic heterogeneity in tumor cells was regulated by both asymmetric division and glucose supply. The increased probability p and inadequate glucose supply enhanced the emergence of quiescent tumor cells. Therefore, phenotypic heterogeneity in tumor cells was temporal–spatial dependent. Figure S4–Fig. S6 (in the supplementary material 1) indicate how many cytotoxic T cells were inactivated by tumor cells in each step. Each column represented the transient number of inactivated T cells at each step in six individual repeated simulations regulated by the distinct joint effects of glucose and asymmetric division. Figure 7a summarizes the frequency distribution of emergence of inactivation of cytotoxic T cells induced by proliferating tumor cells. Among time steps at which inactivation of cytotoxic T cells occurred, frequency of emergence of one inactivated cytotoxic T cells per step was highest, followed by that of two inactivated cytotoxic T cells per step. The number of proliferating tumor cells that were involved in the process of inactivation of T cells was significantly reduced. Figure 7b illuminates that the increased number of quiescent tumor cells played their inhibitory function in emergence of inactivation of cytotoxic T cells per step. Taken together, the smaller number of tumor cells within a tumor mass prone to quiescence was involved in the process of

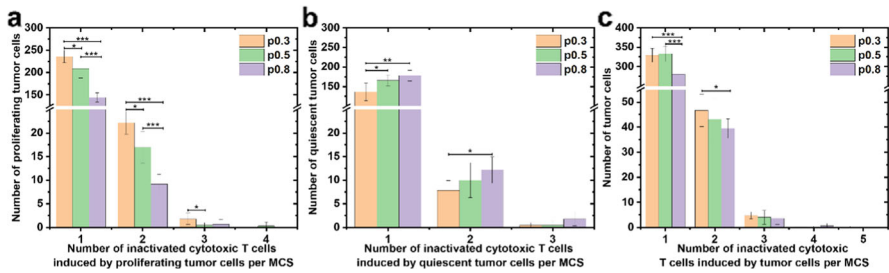


Fig. 7 The frequency distribution of emergence of inactivation of cytotoxic T cells per MCS **a** induced by proliferating tumor cells; **b** induced by quiescent tumor cells; **c** induced by tumor cells. * $P < 0.05$, ** $P < 0.01$, *** $P < 0.001$

inhibiting T cell activity, because the number of proliferating tumor cells decreased more than the number of quiescent tumor cells increased, as shown in Fig. 7c.

To better explore the mechanism responsible for the collective suppressive effect of a tumor mass, we investigated the proportions of the accumulated number of inactivated cytotoxic T cells contributed by two populations of tumor cells. Compared with Fig. 8a, c, the increasing number of inactivated cytotoxic T cells was mainly contributed by quiescent tumor cells from around 440–700 MCS. At the initial stage, adequate nutrient supply was provided to a tumor mass, so the distribution of the quiescent tumor cells was mainly determined by asymmetric division and had higher possibility of appearance at the margin of a tumor mass (Figs. 4, 5a). Thus, quiescent tumor cells could perform their stronger inhibitory function. As the time went on, the suppressive contribution of a population of proliferating tumor cells increased, while a population of quiescent tumor cells exhibited a gradually decreased trend. The contribution of a population of quiescent tumor cells was enhanced but still smaller than that of a population of proliferating tumor cells in the cases of p with the values of 0.3 and 0.5 and greater than that of a population of proliferating tumor cells in the cases of p with the values of 0.8. As indicated in Figs. 4 and 8c, it was concluded that a population of quiescent tumor cells did not sufficiently expose their inhibitory effects on cytotoxic T

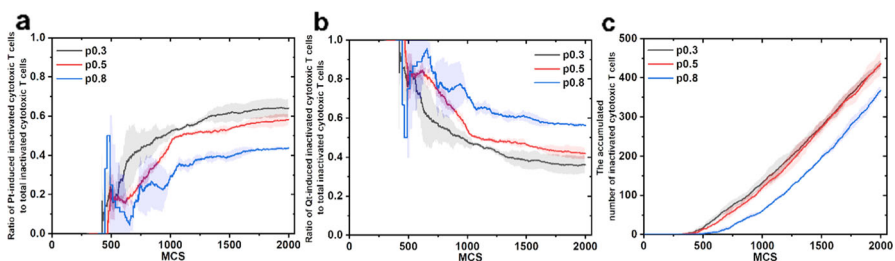


Fig. 8 **a** Ratio of accumulated number of inactivated cytotoxic T cells induced by proliferating tumor cells to the accumulated total number of inactivated cytotoxic T cells; **b** ratio of accumulated number of inactivated cytotoxic T cells induced by quiescent tumor cells to the accumulated total number of inactivated cytotoxic T cells; **c** the accumulated number of inactivated cytotoxic T cells

cells due to their distribution. In the following parts, we would discuss the suppressive capability of a population of quiescent tumor cells.

To better evaluate the suppressive capability of a population of proliferating tumor cells and a population of quiescent tumor cells, tumor cells that exactly inactivated cytotoxic T cells should be sorted from two populations, respectively. Among these effective tumor cells showed distinct individual suppressive effects characterized by the number of inactivated cytotoxic T cells corresponding to the specific cell IDs during the whole simulation time (Fig. S7–S8). Each column represented the number of cytotoxic T cells inactivated by every tumor cell in six individual repeated simulations regulated by the distinct joint effects of glucose and asymmetric division. In Fig. 9a, b, a “non-0” case represents how many tumor cells could accumulatively inactivate cytotoxic T cells during their lifetime, while a “0” case represents tumor cells that did not inactivate cytotoxic T cells during the whole course. A tumor mass prone to quiescence reduced the number of proliferating tumor cells that inactivated cytotoxic T cells and increased that of the quiescent tumor cells. Notably, among a population of proliferating tumor cells predominantly were effective tumor cells that could inactivate only one cytotoxic T cell during the whole course, followed by the cases of two and three cytotoxic T cells (Fig. 9c). Although lower proportion of quiescent tumor cells

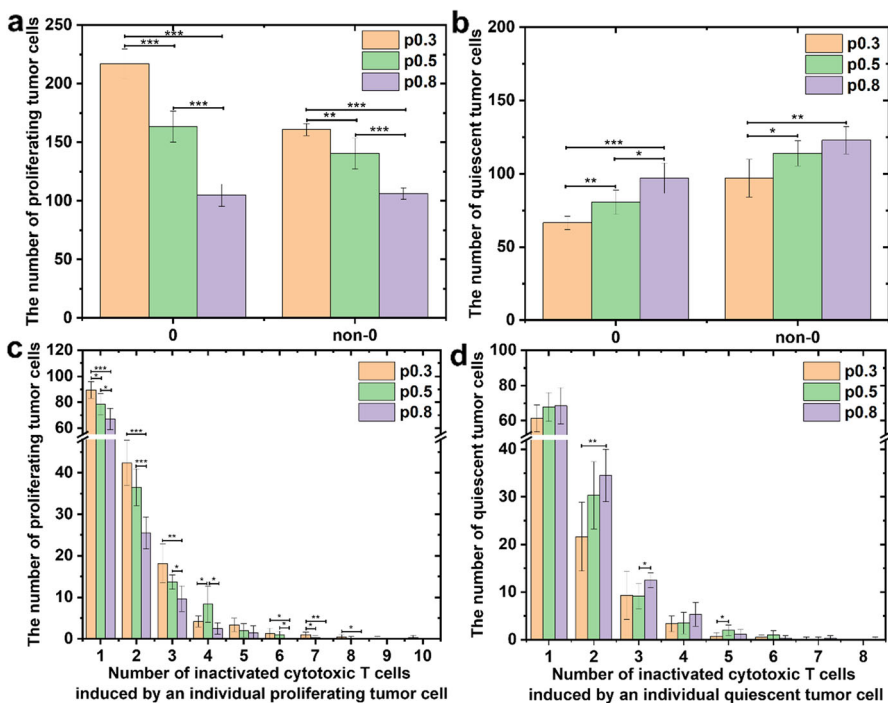


Fig. 9 The distribution statistics of the inhibitory ability of an individual tumor cell in activity of cytotoxic T cells during the simulation time. **a** proliferating tumor cells; **b** quiescent tumor cells; **c** the capability of the population of proliferating tumor cells; **d** the capability of the population of quiescent tumor cells. * $P < 0.05$, ** $P < 0.01$, *** $P < 0.001$

that exactly inactivated cytotoxic T cells, it seemed that the number of quiescent tumor cells that could inactivate more than one cytotoxic T cell increased (Fig. 9d). Thus, the suppressive capability of the population of quiescent tumor cells was enhanced.

In general, increased p weakened the collective suppressive effect of a tumor mass on cytotoxic T cells (Fig. 8c). Although the number of quiescent tumor cells that exactly inactivated cytotoxic T cells increased and the suppressive capability of the population of quiescent tumor cells enhanced, the interior spatial distribution of quiescent tumor cells indicated that the reduced collective suppressive capability of a tumor mass prone to quiescence was predominantly determined by the decreasing number of proliferating tumor cells.

3.6 The Difference in the Collective Anti-apoptotic Behaviors of a Population of Proliferating Tumor Cells and a Population of Quiescent Tumor Cells Induced by Cytotoxic T Cells

The effects of increased p on the collective suppressive role of a tumor mass in cytotoxic T cells have been illustrated in the previous sections. Next, increased p -regulated collective anti-apoptotic behaviors of a tumor mass would be investigated. Cytotoxic T cells released perforin/granzyme B to tumor cells in contact with them to initiate the process of apoptosis of tumor cells. Quiescent tumor cells exhibited higher level of Bcl-2, indicating their stronger anti-apoptotic capabilities. Changes in the concentration of Bcl-2 affected the number of apoptotic tumor cells at the cellular level as shown in Fig. 10a, b. Figure 11a, b exhibits the transient number of apoptotic proliferating/quiescent tumor cells in six independent simulations. It could be obviously indicative of sparser emergence of apoptotic proliferating tumor cells compared with apoptotic quiescent tumor cells. Figure 11c demonstrates the total transient number of apoptotic tumor cells. The increased p reduced the proportion of proliferating tumor cells (Fig. 4b), the corresponding apoptotic proliferating tumor cells

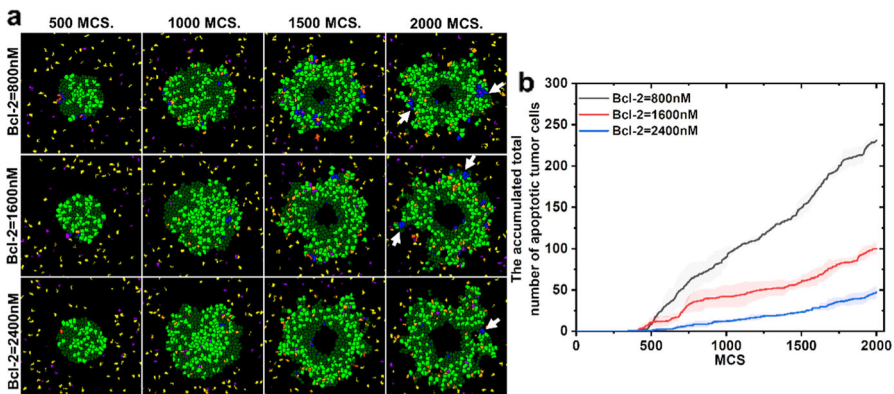


Fig. 10 The difference in the apoptotic behavior of tumor cells with via regulation of Bcl-2. **a** Distribution of tumor cells; **b** the number of apoptotic tumor cells

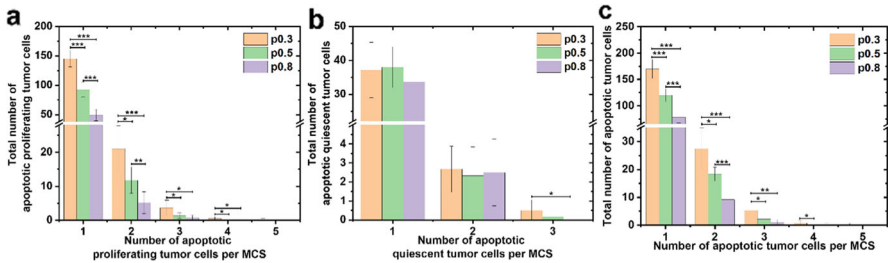


Fig. 11 The frequency distribution of apoptotic tumor cells per MCS. **a** proliferating tumor cells; **b** quiescent tumor cells; **c** total tumor cells. * $P < 0.05$, ** $P < 0.01$, *** $P < 0.001$

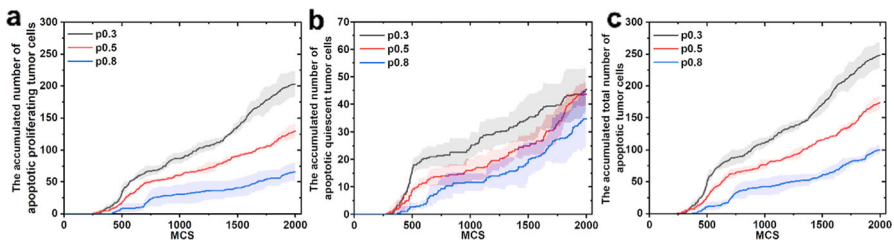


Fig. 12 Changes in the number of apoptotic tumor cells with distinct levels of quiescent tumor cells. **a** The accumulated number of apoptotic proliferating tumor cells; **b** the accumulated number of apoptotic quiescent tumor cells; **c** the accumulated number of apoptotic tumor cells;

became less because proliferating tumor cells had more sensitively apoptotic behaviors (Fig. 12a) and mostly located at the periphery of the tumor mass. Interestingly, the increase of p increased the emergence of a population of quiescent tumor cells, consistent with Fig. 4c, but there was no corresponding increase in the number of the apoptotic quiescent tumor cells (Fig. 12b). Less contact between quiescent tumor cells and cytotoxic T cells could lead to a significant decrease in the number of apoptotic quiescent tumor cells compared with proliferating tumor cells even though higher proportion of quiescent tumor cells could be observed within the tumor mass ($p = 0.8$). Both the insensitive apoptotic behavior of an individual quiescent tumor cell and spatial location of a population of quiescent tumor cells made quiescent tumor cells more likely survive. Therefore, the decrease in the total apoptotic tumor cells as the increase of p was contributed by both a decrease of available proliferating tumor cells and hiding of a population of quiescent tumor cells in the interior region of a mass (Fig. 12c), providing possibility of long-term coexistence of a tumor mass and T cells.

4 Conclusion

The immunotherapy and relapse of malignant tumors are the overwhelming obstacles of tumor treatments mediated by numerous strategies. Among them is the heterogeneity in a tumor mass. In our study, a cellular-level model of tumor–immune interactions

was developed based on the principle of cellular Potts model. The effect of phenotypic heterogeneity in tumors on tumor–immune interactions was investigated. Asymmetric division and glucose distribution jointly regulated the transient changes in the proportion of proliferating/quiescent tumor cells in a solid tumor mass. Glucose supply was quantitatively described based on partial differential equations. Tumor evolution was initiated from a discrete cluster of cells with the attributes described by effective energy terms. Although it was indicated that an individual quiescent tumor cell had stronger anti-apoptotic and suppressive behaviors than a tumor cell in a proliferating state, the outcome of the collective tumor–immune interactions was determined by a temporal–spatial varying population of quiescent tumor cells in a solid tumor mass.

The interactions between the immune system and the tumor as a whole determine the efficiency of immunotherapy. Our model was capable of capturing the changes in interactive profiles triggered by phenotypic heterogeneity in tumors. Complex tumor microenvironment could induce variations in quiescent states of a tumor mass in which different proportion of quiescent tumor cells could be observed. In term of the ability of tumor cells to inhibit T cell function, quiescent tumor cells exhibited higher potential of expression of PD-L1 compared with proliferating tumor cells with exposure to the same amount of IFN- γ . However, IFN- γ was uneven distributed at the cellular level, so the performance of every tumor cell was temporal–spatial dependent. The nonlinear dynamic output “PD-L1” of tumor cells during their lifetime reflected temporal–spatial variance of suppression of T cell function by heterogeneous populations of tumor cells. Similarly, the dynamic apoptotic levels were interpreted by the intracellular network of apoptosis of tumor cells. The difference in the Bcl-2 levels of quiescent and proliferating tumor cells led to the temporal–spatial heterogeneity of the killing capacity of T cells. The incorporation of the intracellular modeling in the interactive behaviors could further explain the temporal–spatial difference in the behaviors of tumor cells within the same population. Therefore, the collective tumor–immune interactions could not be consistent with the interactive dynamics at the single-cell level contributed by the spatial distribution of tumor cells. Our model illustrated that increased p promoted the yield of quiescent tumor cells within a mass, but weakened the collective suppressive effect of a tumor mass on cytotoxic T cells and the apoptotic behavior of a tumor mass. Although quiescent tumor cells did not sufficiently do their inhibitory functions, the possibility of long-term survival was improved due to their interior location within a mass. Hence, a tumor mass with the enhanced quiescent state could adopt the “escape-like” strategy to sustain a population of tumor cells that were more suitable for long-term survival.

Taken together, our simulations for the temporal–spatial effect of phenotypic heterogeneity on the collective tumor–immune interactions indicate that while it is important to identify the efficient targets for enhancing the activity of cytotoxic T cells, it is equally necessary to identify the hidden and long-term factors that may lead to the relapse of tumors. Therefore, although the optimal immunotherapy is likely sufficient to impede tumor progression, the same target may not be as effective if a tumor mass is prone to a quiescence state. Our study provides a potential mechanism for the necessity of targeting a population of quiescent tumor cells in the further development of immunotherapy.

Supplementary Information The online version contains supplementary material available at <https://doi.org/10.1007/s11538-023-01158-z>.

Acknowledgements This work was supported by the Fundament Research Program of Shanxi Province, China (Grant No.: 202203021211176), and Science and technology Innovation project of Higher education institutions in Shanxi Province (Grant No.:19004411) and Shanxi-Zheda Institute of Advanced Materials and Chemical Engineering (Grant Nos.:2021SX-AT008, 2021SX-AT009).

Code availability Code is available in the supplementary material (2).

Declarations

Conflict of interest The authors declare that they have no conflicts of interest.

References

- Adorisio S, Cannarile L, Delfino DV, Ayroldi E (2021) Glucocorticoid and PD-1 cross-talk: Does the immune system become confused? *Cells* 10:2333. <https://doi.org/10.3390/cells10092333>
- Ali A, Hussain M, Ghaffar A et al (2021) Numerical simulations and analysis for mathematical model of avascular tumor growth using Gompertz growth rate function. *Alex Eng J* 60:3731–3740. <https://doi.org/10.1016/j.aej.2021.02.040>
- Alves CP, Dey-Guha I, Kabraji S et al (2018) AKT1low quiescent cancer cells promote solid tumor growth. *Mol Cancer Ther* 17:254–263. <https://doi.org/10.1158/1535-7163.MCT-16-0868>
- Asadullah, Kumar S, Saxena N et al (2021) Combined heterogeneity in cell size and deformability promotes cancer invasiveness. *J Cell Sci* 134:jcs.250225. <https://doi.org/10.1242/jcs.250225>
- Baldominos P, Barbera-Mourelle A, Barreiro O et al (2022) Quiescent cancer cells resist T cell attack by forming an immunosuppressive niche. *Cell* 185:1694–1708.e19. <https://doi.org/10.1016/j.cell.2022.03.033>
- Benchaiib MA, Bouchnita A, Volpert V, Makhoute A (2019) Mathematical modeling reveals that the administration of EGF can promote the elimination of lymph node metastases by PD-1/PD-L1 blockade. *Front Bioeng Biotechnol*. <https://doi.org/10.3389/fbioe.2019.00104>
- Cess CG, Finley SD (2020) Multi-scale modeling of macrophage—T cell interactions within the tumor microenvironment. *PLOS Comput Biol* 16:e1008519. <https://doi.org/10.1371/journal.pcbi.1008519>
- Cooper AK, Kim PS (2014) A cellular automata and a partial differential equation model of tumor–immune dynamics and chemotaxis. In: Eladdadi A, Kim P, Mallet D (eds) *Mathematical models of tumor–immune system dynamics*. Springer, New York, pp 21–46
- de Pillis LG, Radunskaya AE (2014) Modeling tumor–immune dynamics. *Math Models Tumor–immune Syst Dyn*. https://doi.org/10.1007/978-1-4939-1793-8_4
- Dey-Guha I, Wolfer A, Yeh AC et al (2011) Asymmetric cancer cell division regulated by AKT. *Proc Natl Acad Sci* 108:12845–12850. <https://doi.org/10.1073/pnas.1109632108>
- Gao X, Arpin C, Marvel J et al (2016) IL-2 sensitivity and exogenous IL-2 concentration gradient tune the productive contact duration of CD8+ T cell-APC: a multiscale modeling study. *BMC Syst Biol* 10:77. <https://doi.org/10.1186/s12918-016-0323-y>
- Gong C, Milberg O, Wang B et al (2017) A computational multiscale agent-based model for simulating spatio-temporal tumour immune response to PD1 and PDL1 inhibition. *J R Soc Interface* 14:20170320. <https://doi.org/10.1098/rsif.2017.0320>
- Granier C, Vinatier E, Colin E et al (2018) Multiplexed immunofluorescence analysis and quantification of intratumoral PD-1+ Tim-3+ CD8+ T cells. *JoVE J vis Exp*. <https://doi.org/10.3791/56606>
- Grimes DR, Kannan P, McIntyre A et al (2016) The role of oxygen in avascular tumor growth. *PLoS ONE* 11:0153692. <https://doi.org/10.1371/journal.pone.0153692>
- Guisoni N, Mazzitello KI, Diambra L (2018) Modeling active cell movement with the potts model. *Front Phys*. <https://doi.org/10.3389/fphy.2018.00061>
- Hay ZLZ, Slansky JE (2022) Granzymes: the molecular executors of immune-mediated cytotoxicity. *Int J Mol Sci* 23:1833. <https://doi.org/10.3390/ijms23031833>

- Hendratta M, Sudiono J (2016) A computational model for investigating tumor apoptosis induced by mesenchymal stem cell-derived secretome. *Comput Math Methods Med*. <https://doi.org/10.1155/2016/4910603>
- Hsu J-M, Xia W, Hsu Y-H et al (2018) STT3-dependent PD-L1 accumulation on cancer stem cells promotes immune evasion. *Nat Commun* 9:1908. <https://doi.org/10.1038/s41467-018-04313-6>
- Kather JN, Poleszczuk J, Suarez-Carmona M et al (2017) In silico modeling of immunotherapy and stroma-targeting therapies in human colorectal cancer. *Cancer Res* 77:6442–6452. <https://doi.org/10.1158/0008-5472.CAN-17-2006>
- Kim PS, Lee PP (2012) Modeling protective anti-tumor immunity via preventative cancer vaccines using a hybrid agent-based and delay differential equation approach. *PLOS Comput Biol* 8:e1002742. <https://doi.org/10.1371/journal.pcbi.1002742>
- Kleffel S, Schatton T (2013) Tumor dormancy and cancer stem cells: two sides of the same coin? In: Enderling H, Almog N, Hlatky L (eds) *Systems biology of tumor dormancy*. Springer, New York, pp 145–179
- Leschiera E, Lorenzi T, Shen S et al (2022) A mathematical model to study the impact of intra-tumour heterogeneity on anti-tumour CD8+ T cell immune response. *J Theor Biol* 538:111028. <https://doi.org/10.1016/j.jtbi.2022.111028>
- Liao K-L, Bai X-F, Friedman A (2014) Mathematical modeling of interleukin-27 induction of anti-tumor T cells response. *PLoS ONE* 9:e91844. <https://doi.org/10.1371/journal.pone.0091844>
- Liu F, Liu W, Sanin DE et al (2020) Heterogeneity of exhausted T cells in the tumor microenvironment is linked to patient survival following resection in hepatocellular carcinoma. *OncImmunology* 9:1746573. <https://doi.org/10.1080/2162402X.2020.1746573>
- Lyford-Pike S, Peng S, Young GD et al (2013) Evidence for a role of the PD-1:PD-L1 Pathway in immune resistance of HPV-associated head and neck squamous cell carcinoma. *Cancer Res* 73:1733–1741. <https://doi.org/10.1158/0008-5472.CAN-12-2384>
- Pally D, Pramanik D, Hussain S et al (2021) Heterogeneity in 2,6-linked sialic acids potentiates invasion of breast cancer epithelia. *ACS Cent Sci* 7:110–125. <https://doi.org/10.1021/acscentsci.0c00601>
- Phan TG, Croucher PI (2020) The dormant cancer cell life cycle. *Nat Rev Cancer* 20:398–411. <https://doi.org/10.1038/s41568-020-0263-0>
- Phillips T, Simmons P, Inzunza HD et al (2015) Development of an automated PD-L1 immunohistochemistry (IHC) assay for non-small cell lung cancer. *Appl Immunohistochem Mol Morphol* 23:541–549. <https://doi.org/10.1097/PAI.0000000000000256>
- Radunskaya A, Kim R II, TW, (2018) Mathematical modeling of tumor immune interactions: a closer look at the role of a PD-L1 inhibitor in cancer immunotherapy. *Spora J Biomath* 4:25–41. <https://doi.org/10.30707/SPORA4.1Radunskaya>
- Rens EG, Edelstein-Keshet L (2019) From energy to cellular forces in the cellular potts model: an algorithmic approach. *PLOS Comput Biol* 15:e1007459. <https://doi.org/10.1371/journal.pcbi.1007459>
- Risson E, Nobre AR, Maguer-Satta V, Aguirre-Ghiso JA (2020) The current paradigm and challenges ahead for the dormancy of disseminated tumor cells. *Nat Cancer* 1:672–680. <https://doi.org/10.1038/s43018-020-0088-5>
- Robertson-Tessi M, El-Kareh A, Gorieli A (2012) A mathematical model of tumor-immune interactions. *J Theor Biol* 294:56–73. <https://doi.org/10.1016/j.jtbi.2011.10.027>
- Roy M, Finley SD (2019) Metabolic reprogramming dynamics in tumor spheroids: insights from a multicellular, multiscale model. *PLOS Comput Biol* 15:e1007053. <https://doi.org/10.1371/journal.pcbi.1007053>
- Scianna M, Preziosi L (2012) Multiscale developments of the cellular potts model. *Multiscale Model Simul* 10:342–382. <https://doi.org/10.1137/100812951>
- Scianna M, Preziosi L (2013) *Cellular potts models: multiscale extensions and biological applications*. CRC Press, Boca Raton
- Semba T, Funahashi Y, Ono N et al (2004) An angiogenesis inhibitor E7820 shows broad-spectrum tumor growth inhibition in a xenograft model: possible value of integrin $\alpha 2$ on platelets as a biological marker. *Clin Cancer Res* 10:1430–1438. <https://doi.org/10.1158/1078-0432.CCR-0109-03>
- Swat MH, Thomas GL, Belmonte JM et al (2012) Chapter 13—Multi-scale modeling of tissues using CompuCell 3D. In: Asthagiri AR, Arkin AP (eds) *Methods in cell biology*. Academic Press, New York, pp 325–366

- Swat MH, Thomas GL, Shirinifard A et al (2015) Emergent stratification in solid tumors selects for reduced cohesion of tumor cells: a multi-cell, virtual-tissue model of tumor evolution using CompuCell 3D. *PLoS ONE* 10:e0127972. <https://doi.org/10.1371/journal.pone.0127972>
- Tysnes BB, Maurert HR, Porwol T et al (2001) Bromelain reversibly inhibits invasive properties of glioma cells. *Neoplasia* 3:469–479. <https://doi.org/10.1038/sj.neo.7900196>
- Vittadello ST, McCue SW, Gunasingh G et al (2021) A novel mathematical model of heterogeneous cell proliferation. *J Math Biol* 82:34. <https://doi.org/10.1007/s00285-021-01580-8>
- Wen Z, Liao Q, Hu Y et al (2013) A spheroid-based 3-D culture model for pancreatic cancer drug testing, using the acid phosphatase assay. *Braz J Med Biol Res* 46:634–642. <https://doi.org/10.1590/1414-431X20132647>
- Yu J-L, Wei H-C, Jang SR-J (2022) A model of tumor–immune system interactions with healthy cells and immunotherapies. *Math Methods Appl Sci* 45:2852–2870. <https://doi.org/10.1002/mma.7958>
- Zhang X, De Milito A, Olofsson MH et al (2015) Targeting mitochondrial function to treat quiescent tumor cells in solid tumors. *Int J Mol Sci* 16:27313–27326. <https://doi.org/10.3390/ijms161126020>

Publisher's Note Springer Nature remains neutral with regard to jurisdictional claims in published maps and institutional affiliations.

Springer Nature or its licensor (e.g. a society or other partner) holds exclusive rights to this article under a publishing agreement with the author(s) or other rightsholder(s); author self-archiving of the accepted manuscript version of this article is solely governed by the terms of such publishing agreement and applicable law.